
CONSTRAINT-BASED GRAPH NETWORK SIMULATOR

Yulia Rubanova*, Alvaro Sanchez-Gonzalez*, Tobias Pfaff, Peter Battaglia

DeepMind, London, UK

{rubanova, alvarosg, tpfaff, peterbattaglia}@deepmind.com

ABSTRACT

In the rapidly advancing area of learned physical simulators, nearly all methods train forward models that directly predict future states from input states. However, many traditional simulation engines use a constraint-based approach instead of direct prediction. Here we present a framework for constraint-based learned simulation, where a scalar constraint function is implemented as a neural network, and future predictions are computed as the solutions to optimization problems under these learned constraints. We implement our method using a graph neural network as the constraint function and gradient descent as the constraint solver. The architecture can be trained by standard backpropagation. We test the model on a variety of challenging physical domains, including simulated ropes, bouncing balls, colliding irregular shapes and splashing fluids. Our model achieves better or comparable performance to top learned simulators. A key advantage of our model is the ability to generalize to more solver iterations at test time to improve the simulation accuracy. We also show how hand-designed constraints can be added at test time to satisfy objectives which were not present in the training data, which is not possible with forward approaches. Our constraint-based framework is applicable to any setting where forward learned simulators are used, and demonstrates how learned simulators can leverage additional inductive biases as well as the techniques from the field of numerical methods.

1 INTRODUCTION

Consider a bowling ball colliding with a bowling pin. You might explain this event as involving a pair of forces being generated, one which causes the pin to move, and the other which causes the ball to careen away with a different direction and speed. This kind of intuitive cause-and-effect approach is analogous to physical simulators that apply an explicit forward model to calculate a future state directly from the current one, such as when numerically integrating discretized equations of motion.

An alternative, but equally valid, way to explain the collision is in terms of constraint satisfaction: the ball and pin cannot occupy the same location at the same time, and their combined energies and momenta must be conserved. The post-collision trajectories are the only way the future can unfold without violating these constraints. This constraint-based approach is analogous to physical simulators that use an implicit function to model a system of constraints over the current and future states. These simulators generate a prediction by searching for a future state that respects all constraints.

Both families of simulators—those based on explicit, forward functions versus those which define the dynamics implicitly, via constraints—are widely used in physics, engineering, and graphics. In principle they can model the same types of dynamics, however, they differ in the ways they compute their respective predictions. In practice these simulators strike different trade-offs that determine why one or the other is preferred in different domains. For example, explicit methods are popular for large systems with (mostly) independent local effects where space and time derivatives are relatively smooth. The accuracy of explicit simulators can often be increased by discretizing space and time more finely. On the other hand, implicit approaches are often preferred for systems with strong interactions, such rigid and stiff dynamics, and more accurate solutions can often be found by using more sophisticated constraint solvers or by increasing the computational budget (e.g., solver iterations) allocated to searching for solutions. The field of machine learning has recently seen rapid advances in methods for learned simulation, however almost all of these methods have focused

on explicit forward model approaches (e.g., [Sanchez-Gonzalez et al. \(2020\)](#); [Pfaff et al. \(2021\)](#)), with few exceptions ([Yang et al., 2020](#)).

Here we present a framework for learning to simulate complex dynamics via constraint satisfaction. Our “Constraint-based Graph Network Simulator” (C-GNS) defines a single scalar-valued constraint function that represents whether a future state satisfies the learned constraint, conditioned on the current and previous states. Conditioning on the previous states even allows our method to capture the time dynamics within its constraint function. We implement the constraint function as a Graph Neural Network (GNN) ([Bronstein et al., 2017](#); [Battaglia et al., 2018](#)), which can model systems with rich compositional structure, such as multiple bodies, complex meshes, etc. To predict the future state, we use a gradient-based solver that iteratively refines a proposed state to satisfy the constraints. We train by backpropagating loss gradients through the solver.

Crucially, our model is trained directly on observed trajectory data, and does not require knowledge of the true underlying constraints which govern the system dynamics. The learned constraint function does not need to match the form of the data’s true underlying constraints: if both the true and learned constraint functions yield the same solutions, their objective landscapes still may differ (e.g., the learned constraint function may be convex, while the true one may not). The trainable constraint function and the associated solver are merely the inductive biases of the model, based on the assumption that constraint satisfaction can capture a wide range of complex dynamics, such as rigid collisions, non-rigid fluids.

There are several potential advantages to constraint-based learned simulation. First, the constraint function is decoupled from procedure for satisfying it (e.g., gradient descent, in our case), and the user has freedom to choose different solvers or invest different amounts of computation to improve the solution, as we examine in [Results Section 5.3](#). Another potential advantage is that the constraint function’s semantics is explicitly defined (i.e., states that violate the constraint yield higher constraint function values), and it is possible to incorporate additional constraints into the overall constraint function, which we examine in [Results Section 5.4](#). Finally, we speculate that neural-network-based constraint functions may be simpler than the neural networks that directly predict solutions that satisfy all the physical constraints. By rough analogy, for NP-complete problems, evaluating solutions is (thought to be) cheaper than finding solutions.

We tested the C-GNS on a variety of challenging physical simulation domains generated by different simulation engines: rope, bouncing balls, and bouncing irregular rigid shapes ([MuJoCo](#), [Todorov et al. \(2012\)](#)) and splashing fluids ([Flex](#), [Macklin et al. \(2014a\)](#)). We found that the C-GNS’s simulated rollouts were more accurate than a state-of-the-art Graph Net Simulator (GNS) ([Sanchez-Gonzalez et al., 2020](#)) with comparable number of parameters, as well as Neural Projections by [Yang et al. \(2020\)](#). We also demonstrate several unique features of our model. At test time, C-GNS can use additional solver iterations to improve its predictive accuracy, striking desired speed-accuracy trade-offs. Our model can satisfy new, hand-designed constraints introduced at test time jointly alongside its learned constraints. These properties have not been reported previously for explicit forward models or Neural Projections by ([Yang et al., 2020](#)).

2 BACKGROUND AND RELATED WORK

Constraint solvers are central to many physics simulators. Most rigid-body and game engines use constraints to model joints, collision and contact ([Baraff, 1994](#)). They are used for limiting strain in realistic cloth simulation ([Thomaszewski et al., 2009](#)), and are a core component in Eulerian incompressible fluid solvers to solve for pressure ([Chorin, 1967](#)). Recently, position-based ([Müller et al., 2007](#)) and projective dynamics methods ([Bouaziz et al., 2014](#)) have become very popular for interactive simulation. These methods express dynamics purely as constraints, and can simulate a wide range of physical systems from rigid bodies to soft-bodies to fluids ([Macklin et al., 2014a](#)).

In the recent years there has been a rapid growth of machine learning methods for accelerating scientific simulation of complex systems, such as turbulence ([Kochkov et al., 2021](#); [Wang et al., 2020](#)) and aerodynamics ([Thuerey et al., 2020](#); [Zhang et al., 2018](#)). In particular, GNN-based learned simulator is a flexible approach which can model a wide range of systems, from articulated dynamics ([Sanchez-Gonzalez et al., 2018](#)) to particle-based physics ([Mrowca et al., 2018](#); [Li et al., 2019](#); [Sanchez-Gonzalez et al., 2020](#)) and mesh-based continuum systems ([Pfaff et al., 2021](#); [De Avila](#)

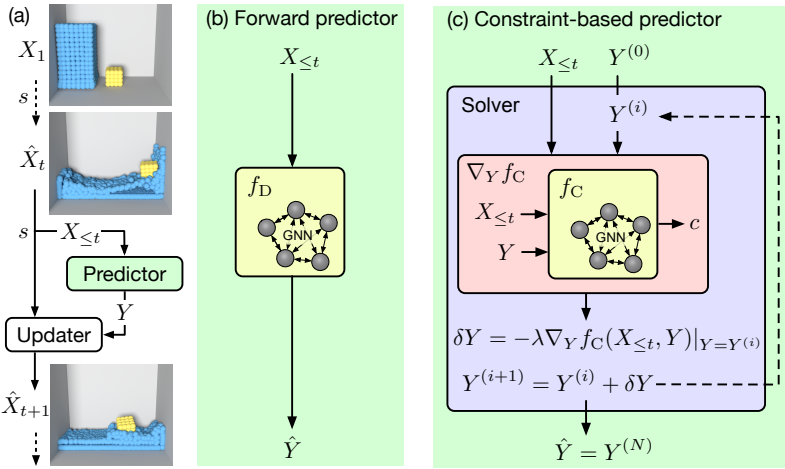


Figure 1: **Learned simulator schematics.** (a) A simulator s maps $X_{\leq t}$ to a future state \hat{X}_{t+1} . The PREDICTOR takes $X_{\leq t}$ and returns \hat{Y} which represents information about the system’s temporal evolution. An UPDATER uses \hat{Y} to update X_t to \hat{X}_{t+1} . (b) Forward GNN simulator. The PREDICTOR maps $X_{\leq t}$ directly to \hat{Y} using f_D . (c) Constraint-based Graph Network simulator (C-GNS). The PREDICTOR iteratively solves for a \hat{Y} to satisfy a constraint function f_C using $\nabla_Y f_C$.

Belbute-Peres et al., 2020), and generalize well to unseen scenarios. Combining learning algorithms with principles from physics and numerical methods, such as auxiliary loss terms and rich inductive biases, can improve sample complexity, computational efficiency, and generalization (Wu et al., 2018; Karniadakis et al., 2021; Chen et al., 2018; Rubanova et al., 2019). Imposing Hamiltonian (Greydanus et al., 2019; Sanchez-Gonzalez et al., 2019; Chen et al., 2019) and Lagrangian (Lutter et al., 2019; Cranmer et al., 2020; Finzi et al., 2020) mechanics in learned simulators offers unique speed/accuracy tradeoffs and can preserve symmetries more effectively.

Recent methods have been proposed for learning constraint functions and solving them in a model’s forward pass (Duvenaud et al. (2020)’s “Deep Implicit Layers” tutorial is an excellent hands-on survey). Such models can play games (Amos & Kolter, 2017; Wang et al., 2019), optimize power flow (Donti et al., 2021), support robotic planning (Loula et al., 2020), and perform combinatorial optimization (Bartunov et al., 2020). Solvers such as gradient descent and Newton’s method are differentiable and support training by backpropagation, but this can be computationally expensive, so approaches such as Deep Equilibrium Models (DEQ) (Bai et al., 2019; 2020) use implicit differentiation to compute gradients only at the solution point.

Despite the popularity of constraint-based traditional simulators, only a single work projects positional variables on a learned constraint manifold has been reported (Yang et al., 2020). See section 4.4 for a detailed comparison between our model and Yang et al. (2020).

3 MODEL FRAMEWORK

3.1 SIMULATION BASICS

A physical trajectory, measured at discrete time intervals, is a sequence of states, (X_1, \dots, X_T) , where X_t may contain properties of elements of the system such as the positions, instantaneous velocities, masses, etc. A physical simulator s is a function that maps current and/or previous state(s), which we term the *context*, $X_{\leq t}$, to a predicted future state, $\hat{X}_{t+1} = s(X_{\leq t})$ (see Figure 1a)¹². A

¹Despite that physics is Markovian, we use $X_{\leq t}$ as input because our framework can also apply to dynamic processes which are non-Markovian. Providing previous states can also often be helpful when there are hidden properties of the system which are only identifiable over a sequence of observed states, for example when a state does not contain instantaneous velocity information, such as in our environments.

²We loosely use the hat notation (e.g. \hat{X}) for the quantities that are predicted by the model.

simulated physical trajectory termed a *rollout* $(X_t, \hat{X}_{t+1} \hat{X}_{t+2}, \dots)$, can be generated by repeatedly applying s to its own predicted state, $\hat{X}_{t+1} = s(X_{\leq t})$.

Simulators are often comprised of a PREDICTOR and an UPDATER mechanism. The PREDICTOR maps the context $X_{\leq t}$ to an update value \hat{Y} that represents information about the system’s temporal evolution at the current time (e.g., new positions, velocities, accelerations, etc.). Then the UPDATER mechanism uses \hat{Y} to update the current state to the next state: $\hat{X}_{t+1} = \text{UPDATER}(X_{\leq t}, \hat{Y})$, e.g. updating current positions and velocities represented by X_t with new velocities and accelerations represented by \hat{Y} to predict the next state.

3.2 EXPLICIT SIMULATORS

Across science, engineering, and graphics, a popular class of simulators (Todorov et al., 2012; Monaghan, 2005; Mirtich & Canny, 1995; Witkin et al., 1990) are defined *explicitly*: the state update \hat{Y} is predicted directly from $X_{\leq t}$ using an explicit forward function, $\hat{Y} = f_D(X_{\leq t})$ (Figure 1(b)).

Among the rapidly growing family of learned simulators, the forward function f_D is typically implemented using a graph neural network (GNN) that allows simulators to scale well to the large graphs of 1000s of nodes and support generalization to systems with different shapes and sizes (Sanchez-Gonzalez et al., 2020; Pfaff et al., 2021; Battaglia et al., 2016). We call the explicit GNN-based model **Forward GNN** (also referred to an GNS in the previous works).

3.3 CONSTRAINT-BASED IMPLICIT SIMULATORS

In this paper we explore the learned simulators based on *implicit* formulations of the dynamics. Instead of predicting the desired state directly, our implicit simulator uses a differentiable constraint function $c = f_C(X_{\leq t}, Y)$, where c is a scalar that quantifies how well a proposed state update Y agrees with $X_{\leq t}$. A future prediction is generated in two stages: 1) apply a solver (gradient descent or a zero-finding algorithm) to find a \hat{Y} that satisfies the constraint function, and 2) use the value \hat{Y} in the UPDATER to update X_t to \hat{X}_{t+1} . Our constraint function f_C is defined as a trainable neural network with a non-negative scalar output. It represents an approximation for all the physical constraints in the system, including the time dynamics.

As illustrated in Figure 1, we formulate our constraint-solving procedure via an iterative method that starts with an initial proposal, $Y^{(0)}$. On the i -th iteration, the solver uses the gradient of f_C w.r.t. Y at the current proposal to compute a change to the proposal, $\delta Y = -\lambda \nabla_Y f_C(X_{\leq t}, Y)|_{Y=Y^{(i)}}$. This δY is then used to revise the proposal to, $Y^{(i+1)} = Y^{(i)} + \delta Y$. This process repeats for N steps, and the final proposal value is treated as the PREDICTOR’s output, $\hat{Y} = Y^{(N)}$.

We define the solution as the minimum of the constraint function $\hat{Y} = \arg \min_Y f_C(X_{\leq t}, Y)$. We use gradient descent with the fixed step size λ to find the solution \hat{Y} . We refer to our Constraint-based Graph Network Simulator with gradient descent solver as **C-GNS-GD**.

This general formulation of constraint-based learned simulation can be trained by backpropagating loss gradients through the solver iterations³. The computational budget of the forward pass can be varied via the number of solver iterations N , as we further explore in Section 5.3.

3.4 EXPLICIT ITERATIVE SIMULATORS

As a hybrid between forward and constraint-based simulators, we also introduce the **Iterative GNN** model. Similar to the constraint-based approach, this model iteratively refines a proposed state update, but directly predicts an output $\delta Y = f_{DI}(X_{\leq t}, \hat{Y})$ at each iteration, instead of as the solution to a constraint function. We use this hybrid model to separately study the effect of pure iterations versus iterative constraint-based optimization (Section 5.3 and Figure B.4).

³Implicit differentiation at the solution point should be applicable as well, and potentially offer computational benefits as mentioned in the Section 2, though we do not explore this direction here.

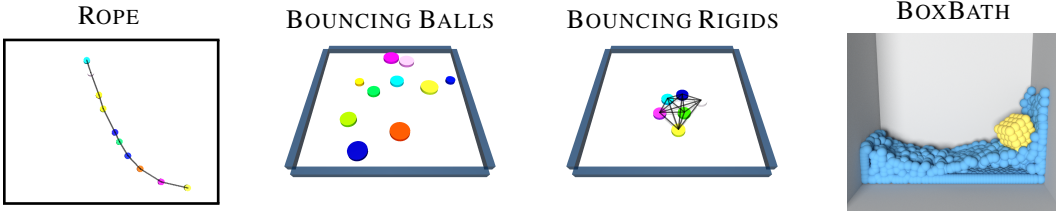


Figure 2: **Renderings of the physical environments.** Videos of the model rollouts are available at: sites.google.com/view/constraint-based-simulator.

4 EXPERIMENTS

4.1 EXPERIMENTAL TASK DOMAINS

We tested our approach on a variety of physical environments, as shown in Figure 2. Our ROPE, BOUNCING BALLS and BOUNCING RIGIDS datasets’ ground truth training and test data were generated by the MuJoCo physics simulator. We also tested on BOXBATH from Li et al. (2019) (1024 particles) to explore the scaling capabilities of the model. These environments involve a diverse set of physical constraints: ‘hard’ constraints (preserving the shape of the rigid object and resolving collisions), and ‘soft’ constraints on fluid movement, handling gravity and preserving the momentum of the rope and bouncing balls.

Representing the physical system Our experimental domains are physical systems comprised of sets of interacting point-like elements, e.g., objects, particles, mesh vertices, etc. The dataset consists of the positions of each element: $P_t = (p_t^j)_{j=1 \dots J}$, where J is the number of elements, and p_t^j is the j -th element’s position at time t . Note that our dataset does not contain the instantaneous velocities, though, as described below, velocity information can be estimated by changes in the position. Additionally, we represent the static properties of the physical elements (masses, material types, etc.) as Z to keep it distinct from the dynamic state information.

4.2 IMPLEMENTATION OF THE C-GNS MODEL

In our implementation the state X_t consists of the positions P_t and the static information Z . The input context is a sequence of the most recent positions and the static properties: $X_{\leq t} := (Z, P_{t-3}, P_{t-2}, P_{t-1}, P_t)$.

To represent the dynamics, we set the update Y to be the change in position over time $V_{t+1} = (v_{t+1}^j)_{j=1 \dots J} \equiv (p_{t+1}^j - p_t^j)_{j=1 \dots J}$, which we informally call “velocity”, estimated as a backward difference. The update mechanism $\hat{X}_{t+1} = \text{UPDATER}(X_{\leq t}, \hat{Y})$ simply becomes $\hat{P}_{t+1} = P_t + \hat{V}_{t+1}$, where \hat{V}_{t+1} is the output of a PREDICTOR.

For BOXBATH, we set the update Y to the acceleration A_{t+1} , for the sake of consistency with Sanchez-Gonzalez et al. (2020). The acceleration is estimated as a backward difference as $A_{t+1} = V_{t+1} - V_t = P_{t+1} - 2P_t + P_{t-1}$. In this case, the UPDATER takes the form $\hat{P}_{t+1} = P_t + V_t + \hat{A}_{t+1} = 2P_t - P_{t-1} + \hat{A}_{t+1}$, where \hat{A}_{t+1} is produced by the PREDICTOR.

GNN-based constraint function We represent the context $X_{\leq t}$ and a proposed update $Y^{(i)}$ as a graph where the nodes of the graph correspond to different elements, such as objects or particles, and the edges correspond to the possible pairwise interactions between them.

When constructing the graph for the context $X_{\leq t}$, we enforce translation-invariance and do not explicitly provide absolute positions P_t as the input to the network. Instead, the features for node j include a sequence of the three most recent position changes (i.e. velocities) $[z^j, v_{t-2}^j, v_{t-1}^j, v_t^j]$, where $v_t^j = p_t^j - p_{t-1}^j$ and z^j are the static properties. To construct the edge feature from node j to k , we provide the relative displacement vector between the nodes’ positions, $e_t^{jk} = p_t^k - p_t^j$. Finally, to represent $Y^{(i)}$, we concatenate the proposed update for node j from the i -th solver iteration $y^{j,(i)}$ (velocity or acceleration) to the node features of the input graph.

We implement the constraint function f_C using a graph network similarly to [Sanchez-Gonzalez et al. \(2018; 2020\); Pfaff et al. \(2021\)](#). We encode nodes and edges of the graph using MLP encoders. Then, we process the graph using a GNN with residual connections for each message-passing layer without global updates. Finally, we use an output decoder to produce a scalar for each node c^j , square these values to make them non-negative and then average them to compute a single scalar c constraint for the entire graph $c = f_C(X_{\leq t}, \hat{Y}) = \frac{1}{J} \sum_{j=1}^J (c^j)^2$.

Optimizing the constraint We initialize $Y^{(0)}$ to the most recent velocity V_t , as we expect this to be a good prior for the future velocity. In the cases when, Y represents the acceleration, we initialize $Y^{(0)}$ to a zero vector. We use auto-differentiation in JAX to compute the constraint gradient $\nabla_Y f_C$. For the gradient descent solver, we use a fixed step size $\lambda = 0.001$. We used $N = 5$ iterations during training.

4.3 TRAINING AND EVALUATION

We train the model on one-step prediction task by computing the L_2 loss between the predicted update \hat{Y} and the corresponding ground truth update, averaged over nodes. Note that it is straightforward to compute the ground-truth update from the dataset. For example, if Y represents the velocity, the update is simply as position difference between the future and previous states in the ground-truth.

We train the model using standard backpropagation with the Adam optimizer. At test time, we compute 1-step metrics by evaluating the 1-step errors along each point of the ground truth trajectory. We also evaluate rollout errors by iteratively applying the learned model starting from an initial state, over 160 rollout steps, and computing the error between the predicted and ground truth trajectories.

4.4 NEURAL PROJECTIONS ([YANG ET AL., 2020](#)) AND RELATED ABLATIONS

The only related work involving learned constraint-based simulation, that we are aware of, is **Neural Projections (NP)** ([Yang et al., 2020](#)). While inspiring the present work, Neural Projections has key differences from our approach, and is fundamentally limited in ways that make it insufficient as a general-purpose learned simulator.

Neural Projections operates directly on the absolute positions of the particles. First, the model uses an Euler step to propose a future position of the particles based on the previous position, estimated velocity and known external forces. Then the model refines the proposal by iteratively projecting it onto a learned constraint manifold, implemented as a multilayer perceptron (MLP). In our framework, this would be equivalent to (1) making the constraint function depend on the update only: $f_C(Y)$ (2) set the optimized update Y to be the future positions of the system $Y := P_{t+1}$ (the UPDATER becomes the identity function) and (3) initialize $Y^{(0)}$ to the output of the Euler step.

Crucially, the Neural Projections constraint function only measures how much the *current* set of proposed positions of the particles violates the learned constraints without context about past states $X_{\leq t}$. Thus, the model cannot correctly resolve the scenarios such as the elastic collisions, as constraint function does not have access to the dynamics (i.e. how the proposed state relates to the previous state, illustrated in [Supplementary Figure A.1](#)). Even if Neural Projections operated over velocities instead of positions, it would still not be able to correctly predict the velocity after an elastic collision without the past context $X_{\leq t}$, because the information about the past velocity is lost after the first solver iteration. This weakness renders Neural Projections insufficient for general-purpose physical simulations. Our model, on the contrary, does not have this issue, because the constraint function is always conditioned on the past context $f_C(X_{\leq t}, Y)$, which allows to model time dynamics as a part of the learned constraint. To study the effect of this difference, we provide an ablation to our model **C-GNS-GD- $f_C(Y)$** that uses only the positional information of the future state and does not have access to the context $X_{\leq t}$ (see details in the [Supplementary Section A.3](#))

Next, Neural Projections defines the constraint solution as $f_C(Y) = 0$, and uses the zero-finding ‘‘Fast Projection’’ (FP) algorithm ([Goldenthal et al., 2007](#)) to find a solution. As described in [Section 3.3](#), our constraint satisfaction problem is defined as minimization, i.e., $\hat{Y} =$

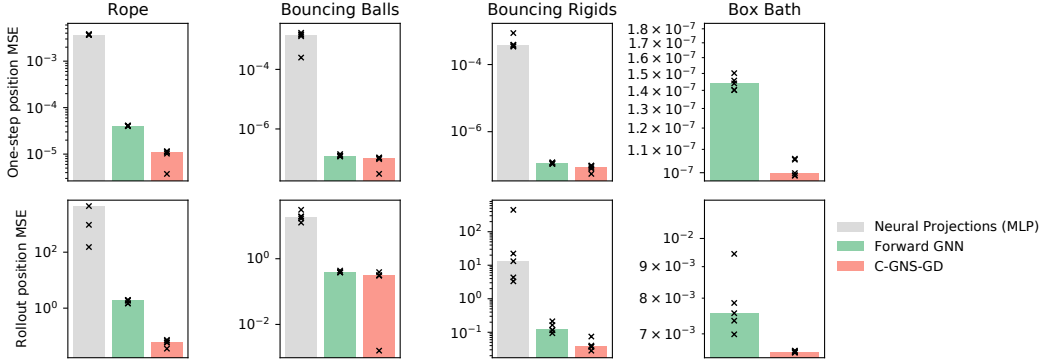


Figure 3: **Comparison to the existing baselines.** Top row: 1-step test MSE on node positions. Bottom row: full-rollout test MSE (160-step). The bar height represents the median MSEs over random seeds. The black cross marks show the MSE metric for each random seed. The black arrows indicate if MSE metric for a random seeds exceeds the upper y limit of the figure. We found Neural Projections could not effectively scale to BOXBATH (see Section 4.4). The y axis is cropped if it exceeds $1e5 \times$ the median MSE of C-GNS-GD.

$\arg \min_Y f_C(X_{\leq t}, Y)$, and solved by gradient descent. To explore these choices, we also tested an FP-based version of our model: **C-GNS-FP**.

Finally, Neural Projections uses an MLP as a constraint function that takes the concatenated features for all of the particles and outputs the constraint value. Compared to GNN-simulators, MLP-based simulators have been shown to be sub-optimal to model particle systems (Battaglia et al., 2016; Sanchez-Gonzalez et al., 2018). The Neural Projection paper (Yang et al., 2020) includes a heuristic parameter sharing scheme to allow variable number of particles, but it requires manually grouping subsets of the state. It is not clear how this heuristic would scale to large systems with dynamically changing interactions. We also created ablated versions of our model using MLPs instead of GNNs: **C-MLP-GD** and **C-MLP-FP**.

5 RESULTS

5.1 COMPARISON TO EXISTING BASELINES

Our experimental results show that our C-GNS-GD’s performance is generally better than the existing baselines on our datasets⁴. Figure 3 demonstrates that C-GNS-GD has the lowest 1-step and rollout MSE across all datasets, compared to Neural Projections (Yang et al., 2020) and Forward GNN (Pfaff et al., 2021) with the comparable number of parameters (see Supplementary Table B.1 for numerical results). Qualitatively, we observed that for Forward GNN with a similar number of parameters, the box in BOXBATH “melts” over time, as the forward model cannot preserve its rigid shape (see [Videos](#)). The comparable C-GNS-GD, by contrast, effectively maintains the rigid shape of the cube. We further investigate the comparison to larger Forward GNN’s with up to five times more parameters in sections 5.3 and 5.6. These results suggest that constraint-based learned simulators are a competitive alternative to explicit, forward learned simulators.

5.2 INTERPRETING THE LEARNED CONSTRAINTS

To better understand the learned f_C functions in the C-GNS-GD, Figure 4 visualizes the node-wise constraint values as a function of Y (proposed average velocity) for different nodes in the ROPE dataset while holding the other nodes’ proposed update Y fixed. We also overlay the sequence of five points that represent the proposed $Y^{(i)}$ steps from the solver where all nodes were jointly optimized. The figure shows the learned f_C has a minimum near the ground truth Y , which the gradient descent steps are able to reach.

⁴Videos of the model rollouts are available at sites.google.com/view/constraint-based-simulator

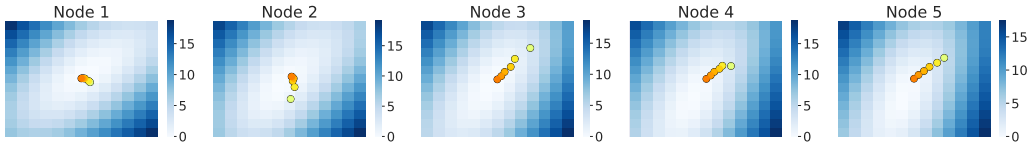


Figure 4: **Visualization of the constraint landscape for a trained C-GNS-GD.** Each subplot corresponds to a different ROPE node. The heatmap’s color shows the constraint value evaluated at different values of Y state. The plot is centered around the ground-truth point. The colored points show the five iterations of the constraint solver, from the initial $Y^{(0)}$ (yellow) to final $Y^{(5)}$ (orange).

5.3 GENERALIZING TO LARGER SYSTEMS VIA INCREASED SOLVER ITERATIONS

A unique feature of our C-GNS-GD model is that the number of solver iterations can be increased to potentially improve the quality of the model’s output. We explore this property on the rope simulation in two settings: on the same dataset used during the training and on a generalization to the ropes with twice as many nodes.

ROPE training distribution We pre-train the C-GNS-GD and Iterative GNN models on the ROPE with $N_{\text{train}} = 5$ iterations and investigate how the test error changes as we vary the number of solver iterations at test time in $N_{\text{test}} \in [0, 15]$ (Figure 5a-b). The test error of C-GNS-GD (light red) decreases as we change the number of iterations from 1 to 5 and then gradually increases as further vary the number of solver iterations up to 15 (by 2 fold for 1-step error). By contrast, Iterative GNN (light blue) overfits to the number of training iterations $N_{\text{train}} = 5$: errors are larger for $N_{\text{test}} \leq 4$ and $N_{\text{test}} \geq 6$ and increases up to 2 orders of magnitude at $N_{\text{test}} \geq 15$.

To further incentivize the Iterative GNN and C-GNS-GD models to be able to handle varied iterations, we trained them with additional loss terms applied to the $Y^{(i)}$ on each solver iteration, instead of only the final proposal $Y^{(N)}$. We used an exponential decay factor, $\alpha = 0.25$ to down-weight the additional loss for earlier solver proposals (see Supplementary Section A.4 for details). The dark blue and red curves in Figure 5a-b show that both Iterative GNN and C-GNS-GD benefit from the additional loss, and specifically the increase in error for C-GNS-GD from 5 to 15 iterations becomes only 8% for one step, and negligible for rollout.

Generalization to a larger system We test if the models can generalize to a rope with twice as many nodes (20 nodes versus 5-10 during training) (Figure 5c-d). Crucially, for C-GNS-GD ($\alpha = 0.25$, dark red), increasing the solver iterations systematically improves the rollout accuracy on the generalization task (by 26.2% on 1-step error in Figure 5(c); 3-fold on the rollout error in Figure 5(d)). Note that this result is achieved with a shallow C-GNS-GD model with 2 message-passing layers that spans 1/10 of the rope length on generalization task. By contrast, the performance of the Iterative GNN with the same number of MP layers (dark blue) stays the same for $N_{\text{test}} > 4$. This demonstrates that C-GNS-GD can leverage extra computational resources at test time, because of the inductive bias that the solver should (approximately) converge to a solution.

Comparison of C-GNS-GD with more solver iterations to Forward GNN First, we compare C-GNS-GD to the Forward GNN with the same number of parameters (2 MP, grey line). We find that the C-GNS-GD has an order of magnitude better performance, both on the training and generalization distribution. Next, we compare to a deeper Forward GNN with 10 MP (black line). Even though the state-of-the-art Forward GNN (10 MP) is competitive and even slightly better on the training distribution (a-b), the C-GNS-GD achieves about 50% lower error when generalizing to the larger system (c-d) by leveraging additional optimization iterations (Figure 5(d)).

In the experiment above we found that by increasing the number of solver iterations N at test time, C-GNS-GD can make use of additional computational resources at test time without re-training or fine-tuning the model and achieve more accurate solutions than non-constraint based models. To our knowledge this is the first demonstration of leveraging additional computation to improve generalization to larger system in the domain of learned physical simulations. This opens exciting

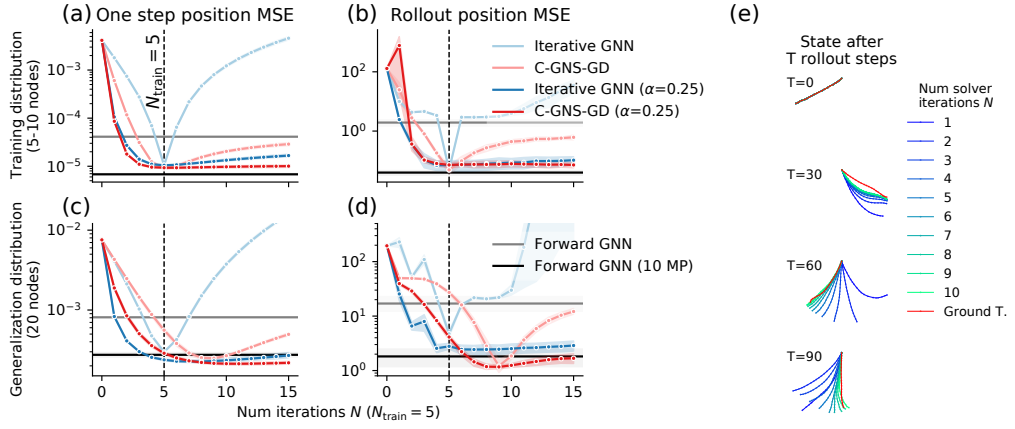


Figure 5: **Generalization to more solver iterations and larger ROPE systems at test time.** (a)-(d)) Top row: test accuracy for ropes with the same lengths as those during training (5-10 nodes). Bottom row: test accuracy for larger ropes (20 nodes) than during training. Left column: 1-step MSE. Right column: full 160-step rollout MSE. The x-axis indicate the number of solver iterations at test time (training used 5 iterations). The y-axis represents MSE values. The horizontal black and grey lines show the performance of the Forward GNN models, which do not have the option to vary the number of iterations at test time. (e) Example of the rollouts from C-GNS-GD with different number of solver iterations.

possibilities to advance the state of the art on training on small, simple systems, and testing on large, complex systems using only a shallow graph network.

5.4 INCORPORATING NOVEL CONSTRAINTS AT TEST TIME

A unique advantage of the constraint-based model is that we can incorporate additional, hand-designed constraints at test time without any fine-tuning on the model. To do so, we simply take a weighted sum of the hand-designed constraints and the learned constraint f_C and run the forward evaluation to find the solution of the combined constraint.

We designed three constraint functions for the ROPE dataset that represent the “forbidden” regions of the space: a vertical wall, a horizontal floor, and a disk-shaped region (see Figure 6). The additional constraint functions are non-negative and increase quadratically as the rope nodes enter the “forbidden” region. We weight the new constraint versus the learned constraint using a hyperparameter. Figure 6 shows how the model predicts the rope will avoid the forbidden regions. In some cases, satisfying the joint constraint resulted in unintuitive behaviors, such as the rope links changing in length to adapt to the obstacle (Videos). This is to be expected, because the minimum of the joint constraint may not overlap with the minimum of the learned constraint, which is the one that would otherwise guarantee length preservation. In cases like this it is the user’s responsibility to tailor the hand-designed constraint to fit the behavior they desire. Here we added a penalty if the relative distances between nodes changes. More broadly, this is a powerful example of how constraint-based models can generalize outside their training data, and solve both for the learned dynamics and arbitrary desired constraints.

5.5 EXAMINING KEY DIFFERENCES FROM NEURAL PROJECTIONS

We demonstrate that our model’s key differences from Neural Projections (Yang et al., 2020) provide substantial improvements in performance. We provide ablations of our C-GNS-GD for each of these differences (conditioning on past states, using GNNs, using gradient descent), as summarized in Table 1. Figure 7 shows that C-GNS-GD has several orders of magnitude lower rollout error compared to Neural Projection, and each of our ablations towards Neural Projection had higher error than C-GNS-GD. Parameterising the constraint function with a GNN instead of an MLP yields the largest improvement on all datasets, particularly on ROPE.

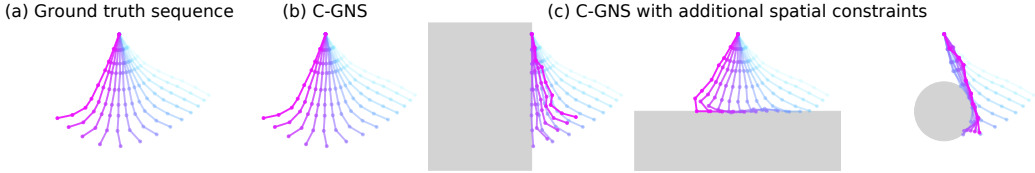


Figure 6: **Adding hand-designed constraints.** (a) The ground truth sequence of rope states, initialized at the cyan-colored state, and simulated over 14 time steps, to the final, purple-colored state. (b) The C-GNS-GD’s rollout, without added constraints. (c) The C-GNS-GD’s rollout, with wall, floor, and disk-shaped “forbidden” zones, imposed at test time via hand-designed constraint functions. A video of the trajectories is available at [Videos](#).

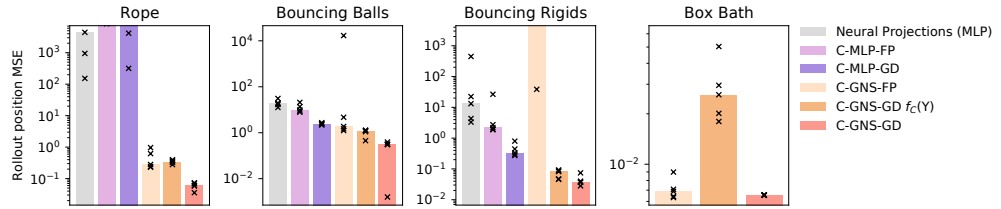


Figure 7: **Ablations to Neural Projections model.** Y axis shows full-rollout test MSE on the node positions. The bar height represents the median MSEs over random seeds. The black cross marks show the MSE metric for each random seed. The black arrows indicates that a random seeds exceeds the upper y limit of the figure. See supplement for 1-step MSE errors. The y axis is cropped if it exceeds $1e5 \times$ the median MSE of C-GNS-GD. The results are not shown for MLP-based models on BOXBATH, as we found that these models could not effectively scale to a large dataset (see Section 4.4).

We found that FP-based models were difficult to train. Notice that the FP models (**C-GNS-FP** and **C-MLP-FP**) suffer from instability across seeds (see “exploding” seeds for C-GNS-FP even on 1-step prediction, marked by a black arrow). We speculate that the FP algorithm makes the training challenging because the step size λ is proportional to f_C . This may cause poor zero-finding early in training when the f_C is not yet informative. Additionally, we find that C-GNS-FP algorithm becomes unstable in the areas with shallow constraint gradients, perhaps because its λ depends on the inverse of the gradient’s norm.

We also report comparisons between the C-GNS-GD and Iterative GNN in Supplementary Figures B.3 and B.2. The Iterative GNN has higher 1-step error than C-GNS-GD on all our datasets and is competitive in terms of the rollout error.

Model variant	f_C	Solution specification	Use $X_{\leq t}$?
Neural Projections	MLP	$f_C = 0$	$f_C(Y)$
C-MLP-FP	MLP	$f_C = 0$	$f_C(X_{\leq t}, Y)$
C-MLP-GD	MLP	$\arg \min f_C$	$f_C(X_{\leq t}, Y)$
C-GNS-FP	GNN	$f_C = 0$	$f_C(X_{\leq t}, Y)$
C-GNS-GD $f_C(Y)$	GNN	$\arg \min f_C$	$f_C(Y)$
C-GNS-GD	GNN	$\arg \min f_C$	$f_C(X_{\leq t}, Y)$

Table 1: **Model ablations.** The “Model variant” column lists the names of Neural Projections, our model, and the ablated models. The “ f_C ” column indicates whether the constraint function was an MLP or GNN. The “Solution specification” column indicates how the solution was defined, i.e., as the zero point or minimum of the constraint function. The “Use $X_{\leq t}$?” column indicates whether or not the constraint function operated over the previous state.

5.6 COMPARISON TO FORWARD GNN ACROSS VARIED NUMBERS OF LAYERS AT TRAIN TIME

We explored how varying the message-passing steps and solver iterations (N) at training time influenced the relative performance of C-GNS-GD compared to Forward GNN in our ROPE dataset (Supplementary Figure B.4). Even when training with one iteration of the solver, C-GNS-GD out-

performs the Forward GNN with the same number of MP layers. The performance further improves if we train the C-GNS-GD model with more iterations (from 1 to 5), while exactly the same number of model parameters is used. In comparison to deeper Forward GNN models (right-most facet), C-GNS-GD with 4 MP layers and 5 iterations has similar 1-step and full rollout MSE to a Forward GNN with 10 MP layers, demonstrating that C-GNS-GD generally require fewer parameters than Forward GNN to achieve comparable performance.

6 DISCUSSION

We presented a general-purpose framework for constraint-based learned simulation, where a learned constraint function implicitly represents the time dynamics of the physical system and future predictions are generated via a constraint solver. We implemented our constraint function as a graph network and used gradient descent as the constraint solver. Our results showed that our C-GNS has competitive or better performance compared to previous learned simulators in a variety of challenging physical simulation problems. We demonstrated unique abilities of C-GNS to generalize to novel, hand-designed constraints and improve the simulation accuracy on larger systems at test time by increasing solver iterations. These properties have not been previously demonstrated in the space of learned physical simulations.

Implicit constraint-based models have stronger inductive biases, compared to explicit forward simulators, which offer trade-offs between expressivity and additional model features, such as adaptive computation and allowing manual constraint terms to be incorporated. One inductive bias is that the constraint-based models impose a parameter-sharing scheme: the gradient $\nabla_Y f_C$ in C-GNS effectively ties the parameters across N solver iterations, analogous to a recurrent neural network. This means that the constraint-based model requires 2.5 times fewer parameters to achieve a comparable test performance to the deep forward simulator with 10 message-passing steps (Section 5.6). However, in principle, a deep forward simulator can be more expressive: each layer’s parameters in the unshared forward model could, after training, take values that are equivalent to the shared parameters of C-GNS. Another inductive bias of the C-GNS comes from how it searches for a solution that converges to the fixed point. This property makes it easy and natural to incorporate novel hand-designed constraints at test time, and generalize to more solver iterations and larger systems.

One key area for further improvements in constraint-based models is the runtime. Our model applies the gradient descent solver in the forward pass and therefore requires approximately $2N$ -times longer computation time compared to the forward model with the same number of parameters, where N is the number of solver iterations. The multiplier 2 is due to the computation of the constraint gradient via vector-Jacobian product (VJP). Similar iterative models, such as Deep Equilibrium models (DEQ, Bai et al. (2019)), suffer similar issues. Different techniques, such as more efficient solvers (with adaptive step or higher-order) or alternative ways to compute the gradient of the constraint solution (e.g., implicit differentiation (Liao et al., 2018), as used in DEQs) may help reduce the runtime and the memory cost.

One area where constraint-based simulation may be especially effective is in systems with hard constraints that would require finding the equilibrium state of many local constraints and might benefit from the adaptive computation. Similarly, domains with global constraints may be easier to train and perform inference in using constraint-based simulators, as it is easier to compute the constraint value than to directly propose the state that satisfies it.

Overall, the performance, generality and unique advantages of constraint-based learned simulation make it an important new direction in the advancement of machine learning methods for complex simulation problems in science and engineering.

REFERENCES

Brandon Amos and J Zico Kolter. Optnet: Differentiable optimization as a layer in neural networks. In *International Conference on Machine Learning*, pp. 136–145. PMLR, 2017.

Jimmy Lei Ba, Jamie Ryan Kiros, and Geoffrey E. Hinton. Layer normalization, 2016.

Shaojie Bai, J Zico Kolter, and Vladlen Koltun. Deep equilibrium models. *arXiv preprint arXiv:1909.01377*, 2019.

Shaojie Bai, Vladlen Koltun, and J Zico Kolter. Multiscale deep equilibrium models. *arXiv preprint arXiv:2006.08656*, 2020.

David Baraff. Fast contact force computation for nonpenetrating rigid bodies. In *Proceedings of the 21st annual conference on Computer graphics and interactive techniques*, pp. 23–34, 1994.

Sergey Bartunov, Vinod Nair, Peter Battaglia, and Tim Lillicrap. Continuous latent search for combinatorial optimization. In *Learning Meets Combinatorial Algorithms at NeurIPS2020*, 2020.

P. Battaglia, Razvan Pascanu, Matthew Lai, Danilo Jimenez Rezende, and K. Kavukcuoglu. Interaction networks for learning about objects, relations and physics. *ArXiv*, abs/1612.00222, 2016.

Peter W Battaglia, Jessica B Hamrick, Victor Bapst, Alvaro Sanchez-Gonzalez, Vinicius Zambaldi, Mateusz Malinowski, Andrea Tacchetti, David Raposo, Adam Santoro, Ryan Faulkner, et al. Relational inductive biases, deep learning, and graph networks. *arXiv preprint arXiv:1806.01261*, 2018.

Sofien Bouaziz, Sebastian Martin, Tiantian Liu, Ladislav Kavan, and Mark Pauly. Projective dynamics: Fusing constraint projections for fast simulation. *ACM transactions on graphics (TOG)*, 33(4):1–11, 2014.

Michael M Bronstein, Joan Bruna, Yann LeCun, Arthur Szlam, and Pierre Vandergheynst. Geometric deep learning: going beyond euclidean data. *IEEE Signal Processing Magazine*, 34(4):18–42, 2017.

Ricky TQ Chen, Yulia Rubanova, Jesse Bettencourt, and David Duvenaud. Neural ordinary differential equations. *arXiv preprint arXiv:1806.07366*, 2018.

Zhengdao Chen, Jianyu Zhang, Martin Arjovsky, and Léon Bottou. Symplectic recurrent neural networks. *arXiv preprint arXiv:1909.13334*, 2019.

Alexandre Joel Chorin. The numerical solution of the navier-stokes equations for an incompressible fluid. *Bulletin of the American Mathematical Society*, 73(6):928–931, 1967.

Miles Cranmer, Sam Greydanus, Stephan Hoyer, Peter Battaglia, David Spergel, and Shirley Ho. Lagrangian neural networks. *arXiv preprint arXiv:2003.04630*, 2020.

Filipe De Avila Belbute-Peres, Thomas Economou, and Zico Kolter. Combining differentiable PDE solvers and graph neural networks for fluid flow prediction. In Hal Daumé III and Aarti Singh (eds.), *Proceedings of the 37th International Conference on Machine Learning*, volume 119 of *Proceedings of Machine Learning Research*, pp. 2402–2411. PMLR, 13–18 Jul 2020.

Priya L Donti, David Rolnick, and J Zico Kolter. Dc3: A learning method for optimization with hard constraints. *arXiv preprint arXiv:2104.12225*, 2021.

David Duvenaud, Zico Kolter, and Matt Johnson. Deep implicit layers - neural odes, deep equilibrium models, and beyond, 2020. URL <http://implicit-layers-tutorial.org/>.

Marc Finzi, Ke Alexander Wang, and Andrew Gordon Wilson. Simplifying hamiltonian and lagrangian neural networks via explicit constraints. *arXiv preprint arXiv:2010.13581*, 2020.

Rony Goldenthal, David Harmon, Raanan Fattal, Michel Bercovier, and Eitan Grinspun. Efficient simulation of inextensible cloth. In *ACM SIGGRAPH 2007 papers*, pp. 49–es. ACM New York, NY, USA, 2007.

Samuel Greydanus, Misko Dzamba, and Jason Yosinski. Hamiltonian neural networks. *Advances in Neural Information Processing Systems*, 32:15379–15389, 2019.

George Em Karniadakis, Ioannis G Kevrekidis, Lu Lu, Paris Perdikaris, Sifan Wang, and Liu Yang. Physics-informed machine learning. *Nature Reviews Physics*, 3(6):422–440, 2021.

Dmitrii Kochkov, Jamie A Smith, Ayya Alieva, Qing Wang, Michael P Brenner, and Stephan Hoyer. Machine learning–accelerated computational fluid dynamics. *Proceedings of the National Academy of Sciences*, 118(21), 2021.

Yunzhu Li, Jiajun Wu, Russ Tedrake, Joshua B Tenenbaum, and Antonio Torralba. Learning particle dynamics for manipulating rigid bodies, deformable objects, and fluids. In *ICLR*, 2019.

Renjie Liao, Yuwen Xiong, Ethan Fetaya, Lisa Zhang, KiJung Yoon, Xaq Pitkow, Raquel Urtasun, and Richard S. Zemel. Reviving and improving recurrent back-propagation. In *ICML*, 2018.

João Loula, Kelsey Allen, Tom Silver, and Josh Tenenbaum. Learning constraint-based planning models from demonstrations. In *2020 IEEE/RSJ International Conference on Intelligent Robots and Systems (IROS)*, pp. 5410–5416. IEEE, 2020.

Michael Lutter, Christian Ritter, and Jan Peters. Deep lagrangian networks: Using physics as model prior for deep learning. *arXiv preprint arXiv:1907.04490*, 2019.

Miles Macklin, Matthias Müller, Nuttapong Chentanez, and Tae-Yong Kim. Unified particle physics for real-time applications. *ACM Transactions on Graphics (TOG)*, 33(4):1–12, 2014a.

Miles Macklin, Matthias Müller, Nuttapong Chentanez, and Tae-Yong Kim. Unified particle physics for real-time applications. *ACM Trans. Graph.*, 33(4), jul 2014b. ISSN 0730-0301. doi: 10.1145/2601097.2601152. URL <https://doi.org/10.1145/2601097.2601152>.

Brian Mirtich and John Canny. Impulse-based simulation of rigid bodies. In *Proceedings of the 1995 Symposium on Interactive 3D Graphics*, I3D ’95, pp. 181–ff., New York, NY, USA, 1995. Association for Computing Machinery. ISBN 0897917367. doi: 10.1145/199404.199436. URL <https://doi.org/10.1145/199404.199436>.

Joseph Monaghan. Smoothed particle hydrodynamics. *Reports on Progress in Physics*, 68:1703, 07 2005. doi: 10.1088/0034-4885/68/8/R01.

Damian Mrowca, Chengxu Zhuang, Elias Wang, Nick Haber, Li Fei-Fei, Joshua B Tenenbaum, and Daniel LK Yamins. Flexible neural representation for physics prediction. *arXiv preprint arXiv:1806.08047*, 2018.

Matthias Müller, Bruno Heidelberger, Marcus Hennix, and John Ratcliff. Position based dynamics. *Journal of Visual Communication and Image Representation*, 18(2):109–118, 2007.

Tobias Pfaff, Meire Fortunato, Alvaro Sanchez-Gonzalez, and Peter Battaglia. Learning mesh-based simulation with graph networks. In *International Conference on Learning Representations*, 2021. URL https://openreview.net/forum?id=roNqYL0_XP.

Yulia Rubanova, Ricky TQ Chen, and David Duvenaud. Latent odes for irregularly-sampled time series. In *Proceedings of the 33rd International Conference on Neural Information Processing Systems*, pp. 5320–5330, 2019.

Alvaro Sanchez-Gonzalez, Nicolas Heess, Jost Tobias Springenberg, Josh Merel, Martin Riedmiller, Raia Hadsell, and Peter Battaglia. Graph networks as learnable physics engines for inference and control. In *International Conference on Machine Learning*, pp. 4470–4479. PMLR, 2018.

Alvaro Sanchez-Gonzalez, Victor Bapst, Kyle Cranmer, and Peter Battaglia. Hamiltonian graph networks with ode integrators. *arXiv preprint arXiv:1909.12790*, 2019.

Alvaro Sanchez-Gonzalez, Jonathan Godwin, Tobias Pfaff, Rex Ying, Jure Leskovec, and Peter Battaglia. Learning to simulate complex physics with graph networks. In Hal Daumé III and Aarti Singh (eds.), *Proceedings of the 37th International Conference on Machine Learning*, volume 119 of *Proceedings of Machine Learning Research*, pp. 8459–8468. PMLR, 13–18 Jul 2020. URL <https://proceedings.mlr.press/v119/sanchez-gonzalez20a.html>.

Bernhard Thomaszewski, Simon Pabst, and Wolfgang Strasser. Continuum-based strain limiting. In *Computer Graphics Forum*, volume 28, pp. 569–576. Wiley Online Library, 2009.

Nils Thuerey, Konstantin Weissenow, Lukas Prantl, and Xiangyu Hu. Deep learning methods for reynolds-averaged navier–stokes simulations of airfoil flows. *AIAA Journal*, 58(1):25–36, 2020.

Emanuel Todorov, Tom Erez, and Yuval Tassa. Mujoco: A physics engine for model-based control. In *2012 IEEE/RSJ International Conference on Intelligent Robots and Systems*, pp. 5026–5033. IEEE, 2012.

Po-Wei Wang, Priya Donti, Bryan Wilder, and Zico Kolter. Satnet: Bridging deep learning and logical reasoning using a differentiable satisfiability solver. In *International Conference on Machine Learning*, pp. 6545–6554. PMLR, 2019.

Rui Wang, Karthik Kashinath, Mustafa Mustafa, Adrian Albert, and Rose Yu. Towards physics-informed deep learning for turbulent flow prediction. In *Proceedings of the 26th ACM SIGKDD International Conference on Knowledge Discovery & Data Mining*, pp. 1457–1466, 2020.

Andrew Witkin, Michael Gleicher, and William Welch. Interactive dynamics. *SIGGRAPH Comput. Graph.*, 24(2):11–21, feb 1990. ISSN 0097-8930. doi: 10.1145/91394.91400. URL <https://doi.org/10.1145/91394.91400>.

Jin-Long Wu, Heng Xiao, and Eric Paterson. Physics-informed machine learning approach for augmenting turbulence models: A comprehensive framework. *Physical Review Fluids*, 3(7):074602, 2018.

Shuqi Yang, Xingzhe He, and Bo Zhu. Learning physical constraints with neural projections. In H. Larochelle, M. Ranzato, R. Hadsell, M. F. Balcan, and H. Lin (eds.), *Advances in Neural Information Processing Systems*, volume 33, pp. 5178–5189. Curran Associates, Inc., 2020. URL <https://proceedings.neurips.cc/paper/2020/file/37bc5e7fb6931a50b3464ec66179085f-Paper.pdf>.

Yao Zhang, Woong Je Sung, and Dimitri N Mavris. Application of convolutional neural network to predict airfoil lift coefficient. In *2018 AIAA/ASCE/AHS/ASC Structures, Structural Dynamics, and Materials Conference*, pp. 1903, 2018.

SUPPLEMENTARY MATERIAL

A IMPLEMENTATION

A.1 THE DATASETS

We generate the ROPE, BOUNCING BALLS and BOUNCING RIGIDS datasets using the MuJoCo physics simulator, with a timestep of 0.001, and recording every 30th time step for our datasets. Our MuJoCo datasets contain 8000/100/100 train/validation/test trajectories of 160 time points each. We show examples of the rollouts for each environment in Supplementary Figure B.1 and [Videos](#).

ROPE The rope is a mass-spring system, where the masses are represented by nodes, and the springs are represented by edges. We randomly sample the number of masses from the discrete interval [5, 10], and the rest length of the springs from the interval [0.6, 1.1]. The springs have effectively infinite stiffness, and thus maintain their rest lengths during the simulation. The rope is fixed in space at one end, and the rest moves under the force of gravity in 2D space.

BOUNCING BALLS The bouncing balls are a 2D particle system confined to a square box, where interactions between the balls, and between the balls and walls, are simulated as rigid collisions. The number of balls is randomly sampled from the discrete interval [5, 10], and the radii of each ball from the interval [0.11, 0.3]. The size of the box is fixed to 5x5 in MuJoCo coordinates.

BOUNCING RIGIDS The bouncing rigidbs are similar to BOUNCING BALLS, except all the balls are connected to each other with rigid bars. We randomly sample the number of balls from the discrete interval [3, 6].

BOXBATH This dataset is from [Li et al. \(2019\)](#), and simulates 3D fluid particle dynamics within a box, with a rigid cube comprised of particles floating on the surface of the fluid, using the NVIDIA FleX physics engine [Macklin et al. \(2014b\)](#). Each simulation contains 960 fluid particles and 64 particles representing the cube. The dataset contains 2700/10/100 training/validation/test trajectories with 150 time steps each.

A.2 CONSTRUCTING THE INPUT GRAPH

We construct the input graph such that the representation is translation invariant, motivated by the idea that the laws of physics do not change based on position in space. To do so, we never provide absolute positions of the nodes in the input to the GNN. Instead, we use velocities (position differences across time) as node features and pairwise position differences between the nodes as edge features, as described below and in the main text. In preliminary work, we found that providing absolute positions to the models causes poorer generalization, especially in larger environments, such as a longer rope.

In BOUNCING RIGIDS and BOUNCING BALLS we use a fully-connected graph. In ROPE we add edges between nodes that are adjacent within the rope. In BOXBATH we add edges between particles that are within a radius of 0.08 from within each other, and then recompute these edges at every step of a rollout according to the updated positions (as in [Sanchez-Gonzalez et al. \(2020\)](#)).

A.2.1 NODE FEATURES

To construct each input node feature, we use the concatenation of the three most recent velocities (position differences) of the node, concatenated with the static parameters (context $X_{\leq t}$): $[z^j, v_{t-2}^j, v_{t-1}^j, v_t^j]$. See Figure B.7(a-b) for experiments with different number of time points. We use five most recent velocities for BOXBATH to match the paradigm in [Sanchez-Gonzalez et al. \(2020\)](#). For the constraint-based models, e.g. C-GNS-GD, we also concatenate the optimized update Y to the node features, as Y represents velocity or acceleration for each node.

We provide an additional one-hot node feature indicating the node type (e.g. rigid, fluid, fixed). For BOUNCING BALLS and BOUNCING RIGIDS, we provide the radius of the object as an additional node feature. Note, because the edges' relative positional displacement and distance features are

computed between centers of the nodes, the model must factor in the object size feature to determine whether a collision is happening.

Handling walls To handle the walls, we include the Euclidean distance between the center of the node to each of wall as additional node features, treating the wall as a plain, similarly to [Sanchez-Gonzalez et al. \(2020\)](#).

We clip the distance to the wall at a fixed maximum value so that this feature cannot be exploited by the network to infer the absolute position within the box. For BOUNCING BALLS and BOUNCING RIGIDS we clip the distance at 2.0, and for BOXBATH at 0.08. For the constraint-based and iterative models, we update the distances to the walls after every step of constraint optimization or iteration, respectively.

A.2.2 EDGE FEATURES

To construct each input edge feature, we use the concatenated displacement vectors $e_t^{jk} = p_t^k - p_t^j$ between the most recent positions at time point t for the nodes j and k connected by the edge. Through the ablation studies, we found that it is sufficient to provide the displacements between the nodes only for the most recent time point t .

For BOXBATH, we also provide the vector norm of the relative distances (not just the vector itself) as an additional edge feature to match [Sanchez-Gonzalez et al. \(2020\)](#).

Note that we do not provide the “rest shapes” (the ground-truth distances of the nodes) for the rigid structures or the rope. When generating a rollout, the model only observes the pairwise displacements/distances between nodes predicted in the previous steps. This makes the rollout prediction more challenging, as the rigid shape might gradually drift from true “rest shape” during the rollout, and there is no way to recover the original shape.

A.2.3 FURTHER DETAILS

Parameterizing the update Y For ROPE, BOUNCING BALLS, BOUNCING RIGIDS we use the velocity (defined as difference between the positions at adjacent time points) as the update Y . At the first iterations, $Y^{(0)}$ is initialized to the previous velocity V_t . For BOXBATH, we use normalized acceleration of the particle as the update Y to better match the approach in [Sanchez-Gonzalez et al. \(2020\)](#); [Pfaff et al. \(2021\)](#). The update $Y^{(0)}$ is initialized to a zero vector on the first iteration. In both cases, the proposed Y is concatenated as an extra node feature at each optimization iteration.

Normalization For BOXBATH we found it was important to normalize inputs and targets to zero-mean unit-variance (as in [Sanchez-Gonzalez et al. \(2020\)](#)). In the other datasets, the scale of the features was already close to zero-mean unit-variance, except for the input/target velocities in BOUNCING BALLS and BOUNCING RIGIDS, so we scaled them by a factor of 100.

Noise To stabilize rollouts in BOXBATH, we added noise to the input sequences in the same manner, and with the same magnitude, as in [Li et al. \(2019\)](#); [Sanchez-Gonzalez et al. \(2020\)](#).

Fixed particles Some of the datasets contain fixed nodes that do not change the position, such as the “pinned” node in the ROPE. As our GNN models are translation invariant, they do not observe absolute positions of the nodes and cannot correct the position of the fixed nodes. Therefore, we prevent the update for the fixed nodes by using *stop_gradient* for gradient-based constraint models, similarly to [Yang et al. \(2020\)](#). For non-constraint-based models, we override fixed particles positions to remain static during a rollout for all models. We also mask out fixed particles from the loss computation. Note that excluding the fixed particles from the predicted output is a standard practice ([Sanchez-Gonzalez et al., 2020](#); [Pfaff et al., 2021](#)).

A.3 MODEL IMPLEMENTATION

Computing the constraint gradients To compute the gradients of the constraint scalars for the batch of graphs, we use the vector-Jacobian product (VJP) function using JAX. VJP does not explic-

itly construct a Jacobian, and its asymptotic computational cost is the same as the forward evaluation of the constraint function.

Constraint function We use the mean aggregation for the per-node outputs $\{c^j | j = 1 \dots J\}$ to obtain the scalar constraint value for the entire graph $c = f_C(X_{\leq t}, \hat{Y}) = \frac{1}{J} \sum_{j=1}^J (c^j)^2$. For gradient descent, we take a square of per-node outputs before aggregating them. For fast projections, we simply take the sum of per-node outputs. We use a fixed learning rate of 0.001 for gradient descent-based constraint solvers. We did not find the model to be very sensitive to this value of the learning rate. We speculate this is because the model can indirectly control the learning rate by learning an arbitrary scaling factor for the constraint.

Fast Projections Fast Projection (FP) algorithm [Goldenthal et al. \(2007\)](#) is a zero-finding algorithm, for constraint functions whose solutions are defined as, $f_C(X_{\leq t}, Y) = 0$. FP uses an adaptive step

$$\lambda = -\frac{f_C(X_{\leq t}, Y^{(i)})}{\|\nabla_Y f_C(X_{\leq t}, Y)|_{Y=Y^{(i)}}\|^2}.$$

Then FP updates the proposed state analogous to our C-GNS-GD model,

$$\delta Y = -\lambda \nabla_Y f_C(X_{\leq t}, Y)|_{Y=Y^{(i)}}$$

$$Y^{(i+1)} = \delta Y + Y^{(i)}$$

For our experiments with Fast Projection, we use $N = 5$ iterations during training, same as for the gradient descent solver.

Forward GNN For the Forward GNN, we use the Graph Network Simulator (GNS) model from [\(Sanchez-Gonzalez et al., 2020; Pfaff et al., 2021\)](#).

The PREDICTOR takes only the context $X_{\leq t}$ and directly outputs the update \hat{Y} . For Forward GNN, the update Y is set to the acceleration $A_{t+1} = V_{t+1} - V_t = P_{t+1} - 2P_t + P_{t-1}$, for consistency with the previous work. Then the update rule in the UPDATER becomes $\hat{P}_{t+1} = P_t + V_t + \hat{A}_{t+1} = 2P_t - P_{t-1} + \hat{A}_{t+1}$.

The graph with the context $X_{\leq t}$ is built similarly to the one for C-GNS-GD. After the graph is processed by the graph network, the model uses a per-node MLP decoder to output the update values for each node $(\hat{y}^j)_{j=1 \dots J}$.

Iterative GNN In the Iterative GNN, the function f_{DI} takes both the context $X_{\leq t}$ and the proposed update $Y^{(i)}$ and outputs a change to the proposed update δY . Then, the model computes the update variable for the next iteration as $Y^{(i+1)} = Y^{(i)} + \delta Y$. The PREDICTOR outputs the update variable from the last iteration $Y^{(N)}$.

The input to the f_{DI} at each iteration i is constructed the same way as in C-GNS. We take the graph representing the context $X_{\leq t}$ and concatenate the proposed update $Y^{(i)}$ to each node vector. We use a GNS model with a per-node decoder from [\(Sanchez-Gonzalez et al., 2020; Pfaff et al., 2021\)](#) to process the input graph and output δY for each node.

We set meaning of the update Y similarly to the C-GNS: Y represents the future velocity V_{t+1} on ROPE, BOUNCING BALLS and BOUNCING RIGIDS; and acceleration A_{t+1} for BOXBATH. The corresponding UPDATER is also the same as in C-GNS (see Section 4.2). For the first iteration, we initialize $Y^{(0)}$ to the most recent velocity V_t , or to a zero vector if Y represents the acceleration (BOXBATH).

C-GNS-GD- $f_C(Y)$ This model is similar to C-GNS-GD, except the past states $X_{\leq t}$ are not provided as part of the input. For this ablation, the model directly optimizes the positional information of the future state, similarly to [Yang et al. \(2020\)](#), rather than velocity or acceleration. Thus, the update Y is set to the positions P_{t+1} , as in the Neural Projections model. The corresponding UPDATER becomes simply an identity function.

To construct the input graph, we use only the positional information of the proposed future state P_{t+1} and static properties Z . Thus, the node features do not include any information about the past states, nor the proposed approximate future velocity $V_{t+1} = P_{t+1} - P_t$. For the edge features, we use the relative displacement vector between the positions of the nodes j and k for the *future* state $e_{t+1}^{jk} = p_{t+1}^k - p_{t+1}^j$.

Neural Projections, C-MLP-FP and C-MLP-GD For the models with MLP-based constraint function we use a similar setup to [Yang et al. \(2020\)](#). We concatenate the features for each node into a single vector and run an MLP to produce a scalar constraint output. For Neural Projections, we include only absolute positions of the nodes into the input. For C-MLP-FP and C-MLP-GD we additionally use the context of the past states, including absolute positions, velocities and distances to the walls for each node. MLP-based models are not provided with explicit pairwise position displacements between the particles, which for the GNN-based models would be in the edge features of the graph. Therefore, we include absolute positions as input to the MLP-based models instead. Next, MLP-based models take a fixed-sized inputs by construction and cannot handle the scenes with variable number of nodes without additional state segmentation schemes. We adapted the MLP-based models to handle scenes with variable number of nodes by padding with zeros up to the maximum state size.

We did not report results for MLP-based models on BOXBATH: MLP models take the concatenated input of node embeddings in order, and on the datasets with 1024 nodes like BOXBATH the model is likely to overfit to the specific ordering of the particles and would be unlikely to yield competitive performance. Additionally, the input vector optimized by the solver would have 1024×32 elements resulting in very small gradients for each element.

A.4 HYPERPARAMETERS

Choice of the number of message-passing layers We chose the smallest possible number of message passing (MP) steps that would allow the C-GNS family of models to solve the task with 5 optimization iterations (2 MP for ROPE, 1MP steps for all other datasets). We then compared this model to a Forward GNN (GNS) with the same architecture and number of parameters for the main result. A full comparison of Forward GNN and C-GNS across multiple values of message passing steps and optimization iterations on ROPE is available in Figure B.4.

For all GNNs, we used a residual connection for the nodes and edges on each message-passing layer. GNNs have only node and edge updates and do not use global updates.

Rope For GNN-based models, we used 2 message-passing steps. We use the latent size of 32 for nodes and edges. The MLPs for processing nodes and edges, as well as node encoder and decoder MLPs, have 3 hidden layers with 256 hidden units each. We used `softplus` activation and a LayerNorm ([Ba et al., 2016](#)).

Bouncing Balls For GNN-based models, we used 1 message-passing step. We use the latent size of 32 for nodes and edges. The MLPs for processing nodes and edges, as well as node encoder and decoder MLPs, have 3 hidden layers with 256 hidden units each. We use `softplus` activation and LayerNorm after every MLP, except the final decoder.

Bouncing Rigid For GNN-based models, we used 1 message-passing step. We use the latent size of 32 for nodes and edges. The MLPs for processing nodes and edges, as well as node encoder and decoder MLPs, have 3 hidden layers with 256 hidden units each. We use `tanh` activation and LayerNorm after every MLP, except the final decoder.

Box Bath For GNN-based models, we used 1 message-passing step. All other hyperparameters are as in [Sanchez-Gonzalez et al. \(2020\)](#). The GNNs’ node and edge function MLPs each had 2 hidden layers with 128 hidden units, and hidden node and edge latent sizes of 128 each. We use `softplus` activation and LayerNorm after every MLP, except the final decoder.

Models with MLP constraints For MLP-based models (Neural Projectons, C-MLP-FP and C-MLP-GD), we used an MLP with 5 hidden layers and 256 hidden units, following the architecture in [Yang et al. \(2020\)](#). We used `softplus` activation with no LayerNorm.

Training We train the models for 1M steps on ROPE, BOUNCING BALLS and BOUNCING RIGIDS. We used the Adam optimizer with an initial learning rate of 0.0001, and a decay factor of 0.7 and applied with a schedule at steps (1e5, 2e5, 4e5, 8e5). We use a batch size of 64. We trained for 2.5M steps for the experiments studying the number of solver iterations. On BOX BATH we trained for 2.5M steps with a batch size of 2, and a learning rate starting at 0.001 and decaying continuously at a rate of 0.1 every 1M steps, as in [Sanchez-Gonzalez et al. \(2020\)](#).

Loss on multiple iterations In section 5.3 we explored training iterative models with a loss imposed on all intermediate outputs $\hat{Y}^{(i)}$ instead of the output of the last iteration $\hat{Y}^{(N)}$ only. We used exponentially decaying relative loss weights (decaying from the final step back to the first), such that the relative weight w_i for the loss term for the $\hat{Y}^{(i)}$ output was $w_i = \alpha^{N-i}$. The goal of α is to encourage the model to make progress towards the minimum at each iteration, without penalizing the model too heavily for not reaching the solution in few iterations. The results with different choices of α are provided on Supplementary Figure B.6.

A.5 LIMITATIONS OF “NEURAL PROJECTIONS” ([YANG ET AL., 2020](#))

The Neural Projections (NP) by [Yang et al. \(2020\)](#) is another approach involving learned constraint-based simulation. However, it has several fundamental limitations that make it insufficient as a general-purpose learned simulator. Here we elaborate on these limitations, briefly described in the main text.

Limitation of static constraints The learned constraint in NP model depends only on the proposed future positions (i.e. the “static” state). Thus, NP cannot represent constraints that depend on two or more states across time by construction. For example, NP’s constraint function on its own cannot model the time dynamics of a single particle with constant velocity, which is presumably why NP applies an Euler step to initialize the first proposal that is passed to the constraint solver. NP is also in principle not well suited to model elastic collisions properly, as illustrated in Figure A.1. In the top scenario, the Euler step proposes the ball moves past the thin wall. Since NP’s constraint function does not regard this as a constraint violation, the ball will continue moving ahead as if the wall does not exist. In the bottom scenario, the Euler step places the ball within the wall, and because the nearest constraint-satisfying position for the ball is at the edge of the wall, the approach would, in principle, only correct the position of the ball until the ball stops overlapping the wall as the solution, leaving the ball right next to the wall, regardless of the ball’s initial position and velocity before the wall collision.

More generally, NP cannot enforce constraints or symmetries defined over time, such as energy preservation: once the Euler step breaks energy preservation, the proposed future state does not contain enough information about the energy of the previous state to be able to identify a constraint violation and resolve it in a way that is consistent with the true dynamics.

Neural Projection also incorporates external forces, such as gravity, by directly updating the velocities before the Euler step, which is probably necessary because, again, NP’s constraint function cannot enforce external effects which involve time (e.g., force and acceleration relate to the second *time* derivative of the position). This is a strong assumption: it means NP must be provided with such temporal effects explicitly, along with the appropriate hard-coded update mechanism, outside of the learnable part of the architecture. Similar to these examples, there are many other types of dynamics that cannot be expressed as constraint satisfaction over the predicted state from an initial Euler proposal, so overall NP cannot be considered a general-purpose learned simulator.

By contrast, because our approach’s constraint function takes both the proposed future state and history as input, i.e., $f_C(X_{\leq t}, Y)$, our method can, in principle, capture any time dynamics which explicit forward simulators can.

Hard-coded Euler step NP relies on an Euler step to generate the initial proposed future state for the solver. Given that forward Euler is a relatively inaccurate integrator, when the Euler proposal is

not accurate, the constraint function’s lack of access to the previous state makes it difficult for NP to recover.

In our approach, the initial proposal to the solver is less important, because the constraint function can capture all aspects of the dynamics. For this reason, we simply initialized the proposal to the most recent velocity given as input (or zero acceleration for BOXBATH). However it is possible to generate initial proposals accounting for external forces or a more sophisticated dynamics prediction mechanism (e.g., an explicit forward simulator).

MLP network and the hard-coded grouping technique NP uses an MLP network as the constraint function, and serializes and concatenates all input features into a vector before passing to the MLP. Generally this approach is not scalable to even moderately large systems (e.g., the ≥ 1000 nodes in BOXBATH) or systems which vary greatly in size (thus requiring significant padding), for similar reasons that serializing images and passing them to an MLP is inferior to CNN- and Transformer-based methods.

[Yang et al. \(2020\)](#) do present a scheme for grouping subsets of the input state and passing them to a shared constraint MLP, which is likely intended to overcome the above weakness, however this is more of a heuristic that takes a partial step toward a more mainstream, full-fledged sharing approach, such as our GNN constraint function.

Lack of translation and permutation equivariance. One of the fundamental properties for modeling physical dynamics is translation equivariance, as the laws of physics do not change based on position in space. Similarly, bodies in a physical system are equivariant to permutations: re-indexing them does not affect the dynamics. [Yang et al. \(2020\)](#)’s implementation of NP lack inductive biases for translation and permutation equivariance, which may lead to poor sample complexity of learning and overfitting.

Zero-finding Fast Projections algorithm NP uses the Fast Projection (FP) algorithm ([Goldenthal et al., 2007](#)) to find zero points in its constraint function. In practice we found that using FP, i.e., in our C-MLP-FP and C-GNS-FP model variants, to train less stably across seeds, and harder to train with deeper networks (see the variance of random seeds in Figure 3, and trends in Figure B.5). We speculate that because FP’s step size is proportional to ratio of the constraint function’s value over the squared norm of its gradient, if, early in training, the learned constraint value is large and/or the constraint gradient norm is small, the FP algorithm may take large steps which contribute to the unstable training.

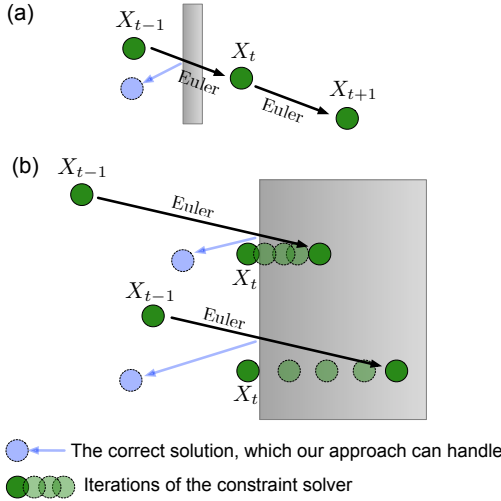


Figure A.1: Failure cases of Neural Projections (Yang et al., 2020)

(a) Collision with a thin wall. The Euler step in NP would propose that the ball moves through the wall. Because NP's constraint $f_C(\text{Euler}(X_{t-1}))$ depends only on the state proposed by the Euler step, it cannot determine that there was a collision between time points $t - 1$ and t . The ball will remain on the other side of the wall and will continue moving forward in later time steps.

(b) Collision with a thick wall. The Euler step in NP would propose that the ball moves into the wall, which should violate the learned constraint. The constraint-solver in NP would then move the ball to the nearest point where the constraint is not violated – the position where the ball touches the wall. As the constraint operates only on the position of the ball, but not on the previous positions or velocities, the ball would always be predicted as just touching the wall, rather than bouncing off the wall.

B SUPPLEMENTARY PLOTS AND TABLES

B.1 EXAMPLES OF MODEL ROLLOUTS FROM C-GNS-GD MODELS

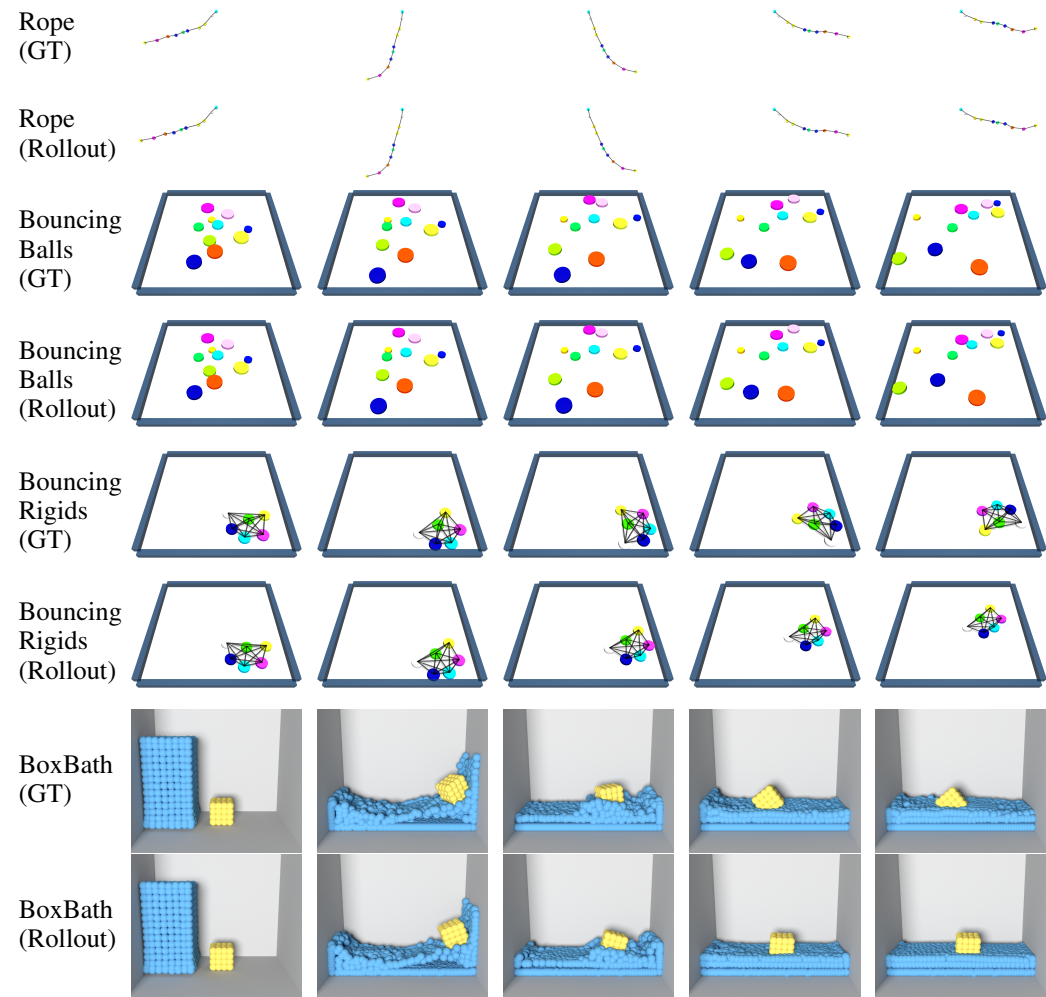


Figure B.1: Examples of the rollouts from C-GNS-GD models for our simulation environments.

B.2 ABLATIONS TO EXISTING BASELINES

Figure B.2 demonstrates the comparison of C-GNS-GD to Forward GNN and Iterative GNN. Adding iterative refinement of the state, but computing the update directly (Iterative GNN) improves 1-step error on ROPE and BOXBATH, but suffers from higher variance across seeds on BOUNCING BALLS and BOUNCING RIGIDS. Computing the update via constraint gradient (C-GNS-GD, ours) further improves 1-step error and improves the model stability. Both Iterative GNN and C-GNS-GD outperform Forward GNN on the full rollout.

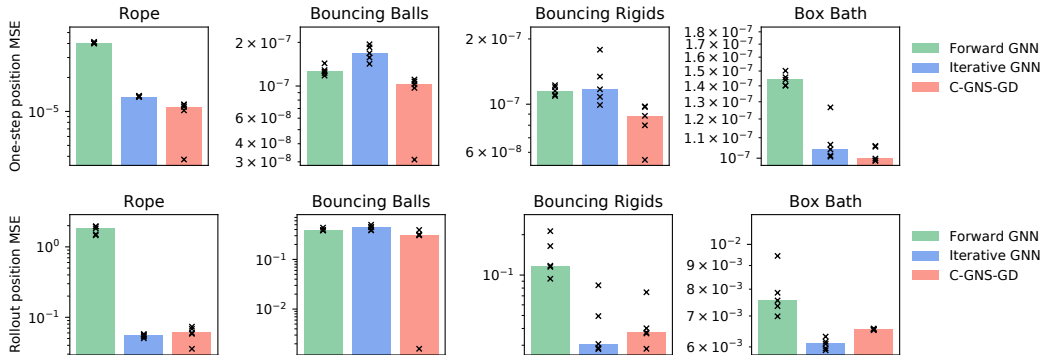


Figure B.2: Comparison to Forward GNN and Iterative GNN. Top row: one-step test MSE error on node positions. Bottom row: full 160-step rollout MSE. The bar height represents the median MSEs over random seeds. The black cross marks show the MSE metric for each random seed. The black arrows indicates that a random seeds exceeds the upper y limit of the figure.

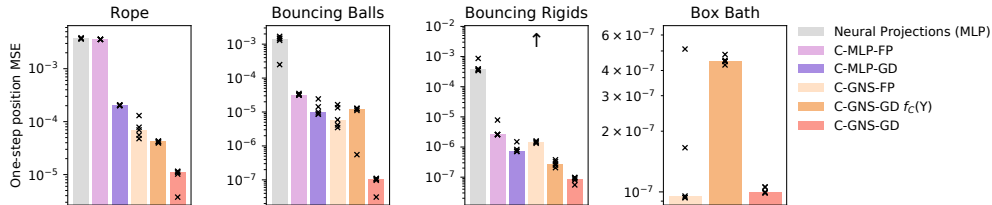


Figure B.3: **Ablations to Neural Projections.** One-step test MSE error on node positions. See Figure 7 for full rollout MSE. The bar height represents the median MSEs over random seeds. The black cross marks show the MSE metric for each random seed. The black arrows indicates that a random seeds exceeds the upper y limit of the figure. The upper y is set to $10^5 \times$ the median MSE of C-GNS-GD.

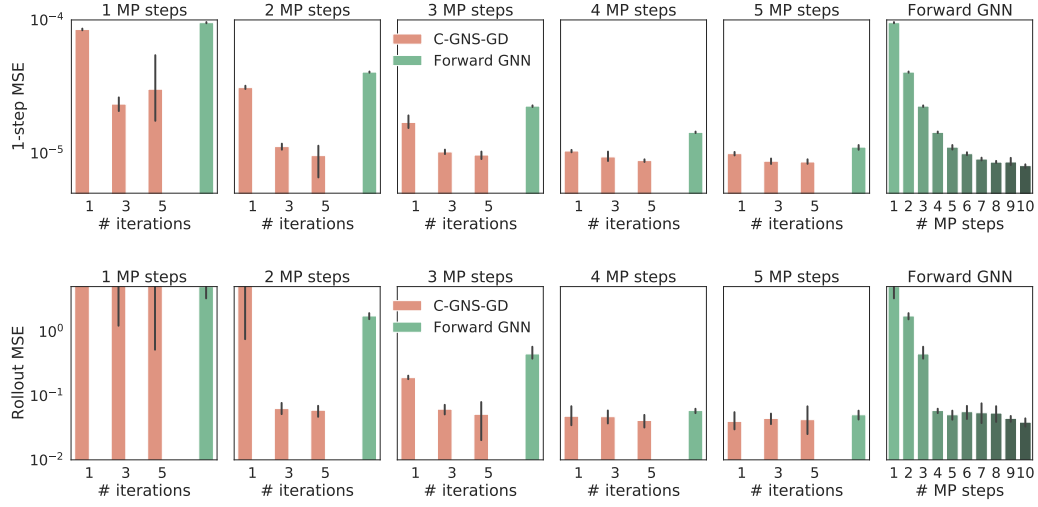


Figure B.4: Test MSE error on ROPE as a function of message-passing (MP) steps and solver iterations. Top row: 1-step test MSE error. Bottom row: full rollout test MSE error. The left five subplots shows performance of C-GNS-GD for different numbers of message-passing steps and different number of solver iterations during training. The green bars show the Forward GNN (it does not use solver iterations). The rightmost subplot shows the Forward GNN with 1 to 10 MP steps.

Table B.1: Median performance of the models on different datasets. The standard deviation from the median is shown over 5 random seeds. We do not show the results for the models where the median value, or standard deviation is more than 1000 times larger than the best model in each column. Note that the tables use different scales to demonstrate the errors on 1-step error, 10-step rollouts and full rollouts. Results are not shown for MLP models on BOXBATH. We omit the results for the models where the median error is more than 4 orders of magnitude larger than the median error of the C-GNS-GD model.

Model	One-step position MSE			
	Rope (1e-5)	Bouncing Balls (1e-6)	Bouncing Rigid (1e-7)	Box Bath (1e-7)
Neural Projections	370.525 ± 6.120	1434.830 ± 547.491	—	—
ConstraintMLP-FP	358.292 ± 0.532	31.984 ± 1.617	26.009 ± 23.440	—
ConstraintMLP-GD	20.422 ± 0.271	9.965 ± 6.745	7.313 ± 3.443	—
C-GNS-FP	6.983 ± 2.965	5.896 ± 5.930	—	0.954 ± 1.885
C-GNS-GD $f_C(Y)$	4.198 ± 0.137	12.241 ± 5.264	2.697 ± 0.613	4.443 ± 0.182
Forward GNN	4.062 ± 0.050	0.126 ± 0.009	1.152 ± 0.051	1.440 ± 0.038
Iterative GNN	1.355 ± 0.012	0.168 ± 0.019	1.172 ± 0.298	1.042 ± 0.103
C-GNS-GD	1.097 ± 0.326	0.103 ± 0.032	0.884 ± 0.163	0.998 ± 0.038

Model	Rollout position MSE (10 steps)			
	Rope (1e-4)	Bouncing Balls (1e-5)	Bouncing Rigid (1e-5)	Box Bath (1e-5)
Neural Projections	9798.580 ± 176.505	—	—	—
ConstraintMLP-FP	9558.814 ± 9.186	704.608 ± 16.157	48.944 ± 392.478	—
ConstraintMLP-GD	41.000 ± 5.062	756.406 ± 177.790	6.933 ± 3.332	—
C-GNS-FP	44.577 ± 23.233	661.722 ± 372.490	—	0.200 ± 0.321
C-GNS-GD $f_C(Y)$	18.399 ± 1.090	615.769 ± 298.710	0.927 ± 0.279	43.099 ± 14.758
Forward GNN	275.851 ± 73.352	2.853 ± 0.277	12.168 ± 3.459	0.386 ± 0.061
Iterative GNN	2.506 ± 1.454	2.260 ± 0.429	2.380 ± 0.257	0.174 ± 0.020
C-GNS-GD	2.222 ± 0.590	0.613 ± 0.333	2.482 ± 0.384	0.288 ± 0.055

Model	Rollout position MSE			
	Rope (1e-1)	Bouncing Balls	Bouncing Rigid (1e-1)	Box Bath (1e-2)
Neural Projections	—	18.881 ± 6.131	—	—
ConstraintMLP-FP	—	9.777 ± 5.367	21.828 ± 109.082	—
ConstraintMLP-GD	—	2.425 ± 0.190	3.332 ± 2.164	—
C-GNS-FP	2.804 ± 3.432	—	—	0.689 ± 0.099
C-GNS-GD $f_C(Y)$	3.427 ± 0.400	1.221 ± 0.350	0.818 ± 0.229	2.596 ± 1.189
Forward GNN	18.305 ± 2.340	0.389 ± 0.022	1.174 ± 0.486	0.756 ± 0.089
Iterative GNN	0.546 ± 0.026	0.445 ± 0.044	0.306 ± 0.253	0.609 ± 0.015
C-GNS-GD	0.602 ± 0.131	0.308 ± 0.142	0.374 ± 0.171	0.654 ± 0.002

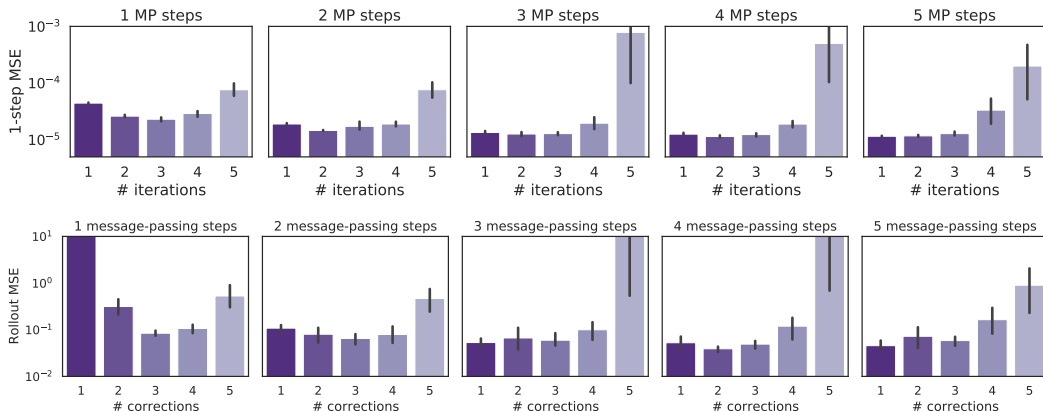


Figure B.5: Test 1-step MSE and Full Rollout MSE of the C-GNS with Neural Projection with different number of message-passing layers and number of constraint solver iterations on the Rope dataset. Top row: position MSE on the full rollout.

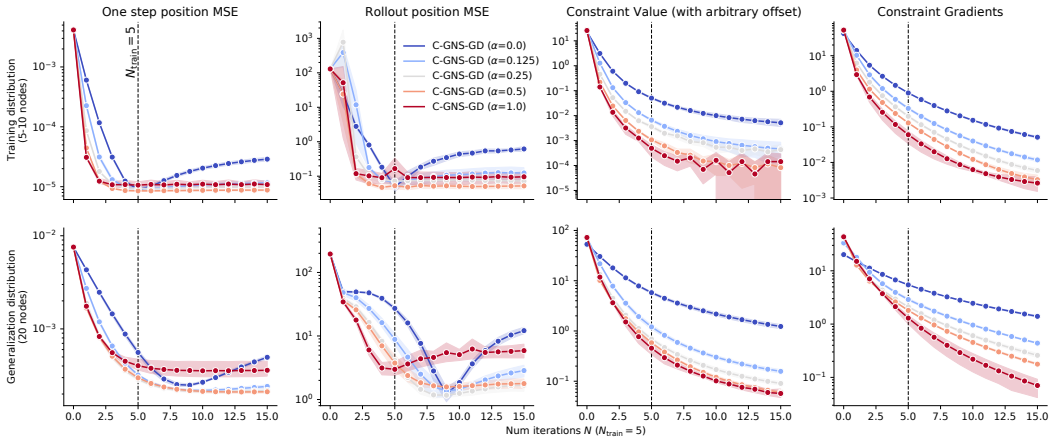


Figure B.6: Generalization to more solver iterations at test time N as function of α . Imposing loss only at the last iteration ($\alpha=1$), causes the model to

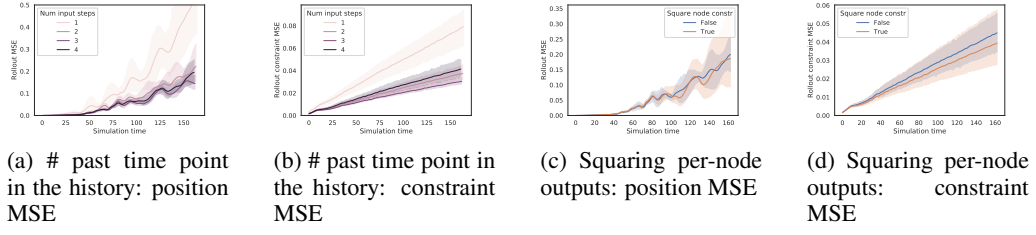


Figure B.7: Ablations of the modelling choices on the ROPE dataset.